





Cite this: DOI: 10.1039/c9en00876d

Structural transformation of sulfidized zerovalent iron and its impact on long-term reactivity†

Marco C. Mangayayam,  ^{*a} Jeffrey Paulo H. Perez,  ^{bc} Knud Dideriksen,  ^d
Helen M. Freeman,  ^{be} Nicolas Bovet,  ^{af}
Liane G. Benning  ^{bc} and Dominique J. Tobler  ^{*a}

Sulfidized nanoscale zerovalent iron (S-nZVI), synthesized *via* two-step synthesis using Na₂S, is an emerging *in situ* material for groundwater remediation, composed of a metallic iron core and iron sulfide shell. The shell efficiently transfers electrons from the core to its surface for contaminant reduction, while simultaneously protecting the core from anoxic corrosion. However, what controls the S-nZVI longevity is poorly understood. In this study, we characterized at high resolution the structure of S-nZVI and assessed its reactivity with trichloroethene (TCE) with increasing aging. Our data of freshly synthesized material show that the S-nZVI shell primarily consists of ~5 nm-thick nanocrystalline mackinawite (FeS_m) with structural imperfections and heterogeneous crystal orientations. As S-nZVI was aged in anoxic artificial groundwater for up to 180 days, the shell remained mostly intact, while the iron core significantly corroded, resulting in hollow particle structures. We interpret that FeS_m defects caused the deterioration of the core. Between 0 and 120 days of aging, rate constants for TCE reduction decreased by only ~41%. This shows that FeS_m remained accessible for TCE reduction; but as the core became depleted, the reduction rate decreased. Re-spiking experiments with TCE oxidized ~1/4 of the core while the FeS_m structure was unaffected. This indicates that the FeS_m does not oxidize during TCE reduction, but merely transfers the electron from the core. Overall, these results demonstrate that S-nZVI is able to sustain its reactivity over extended periods due to the persistence of FeS_m against oxidation, while its defects control the extent of core corrosion.

Received 1st August 2019,
Accepted 8th October 2019

DOI: 10.1039/c9en00876d

rsc.li/es-nano

Environmental significance

Sulfidized nanoscale zerovalent iron (S-nZVI) has been shown to efficiently degrade contaminants for *in situ* groundwater remediation applications. Yet, less is known about the S-nZVI core-shell structure and how this heterogeneous architecture transforms once exposed to groundwater conditions. This is important as it gives insights into the stability of S-nZVI under relevant environmental settings thereby elucidating the key surface processes that permit S-nZVI to sustain reactivity over prolonged periods.

1. Introduction

A large number of studies show that sulfidation of nanoscale zerovalent iron (S-nZVI) with sodium sulfide (Na₂S) enhances

the removal of a range of groundwater contaminants compared to non-sulfidized nanoscale ZVI (nZVI).^{1–5} This enhanced reactivity depends on the used S/Fe ratio during sulfidation, which seems to control the thickness and structure of the iron sulfide shell that forms around the metallic iron (Fe⁰) core.^{3,4} The shell is suggested to have conductive properties, allowing for electron transfer from the Fe⁰ core to the S-nZVI surface.^{1,3,4} Synergistically, the shell limits oxidation of the Fe⁰ core by water (*i.e.*, anoxic corrosion), thus decreasing loss of electrons compared to nZVI,⁶ which in turn gives S-nZVI higher longevity in groundwater settings.

Despite the extensive literature on S-nZVI, surprisingly, we still know very little about the nature of this iron sulfide shell and how it enables such efficient contaminant reduction, particularly after prolonged exposure to anoxic

^a Nano-Science Center, Department of Chemistry, University of Copenhagen, Universitetsparken 5, 2100 Copenhagen, Denmark.

E-mail: mc.marco@chem.ku.dk, dominique.tobler@chem.ku.dk

^b GFZ German Research Center for Geosciences, Telegrafenberg, 14473 Potsdam, Germany

^c Department of Earth Sciences, Free University of Berlin, 12249 Berlin, Germany

^d Geological Survey of Denmark & Greenland (GEUS), Øster Voldgade 10, 1350 Copenhagen, Denmark

^e School of Chemical and Process Engineering, University of Leeds, Leeds, LS2 9JT, UK

^f Danish Hydrocarbon Research and Technology Centre (DHRTC), Technical University of Denmark, Kongens Lyngby, Denmark

† Electronic supplementary information (ESI) available. See DOI: 10.1039/c9en00876d

waters and contaminants. Some initial characterization using high-resolution X-ray diffraction (XRD) has shown that the shell consists of poorly crystalline mackinawite (FeS_m) with an expanded basal plane spacing.² The chemical composition of this FeS_m shell structure has been confirmed by X-ray photoelectron spectroscopy (XPS) and energy-dispersive X-ray spectroscopy (EDXS),^{4,7} and its low reactivity with water has been demonstrated by low H_2 formation rates.^{4,6} In terms of S-nZVI longevity, Fan *et al.*⁶ observed that when S-nZVI was aged for 21 days in deoxygenated, deionized water, its reactivity with indigo carmine decreased by only ~5–10%, with little indication of Fe^0 corrosion during these 21 days. When S-nZVI is aged for longer time spans, however, the Fe^0 core becomes substantially corroded and S-nZVI reactivity decreases more profoundly as demonstrated by Xu *et al.*⁵ Specifically, they reported a ~45% decrease in Fe^0 content and ~50% decrease in trichloroethene reduction rate for S-nZVI aged for 60 days in deoxygenated, deionized water. Similarly, Fan *et al.*² showed that S-nZVI aged with pertechnetate (TcO_4^-) for 2 months led to hollow S-nZVI particles with depleted Fe cores. To compare, nZVI, the current state of the art reductant particle in groundwater remediation, exhibited substantial corrosion and complete loss in TCE reactivity after only 1–2 weeks of aging in anoxic waters.^{5,8,9} While these studies clearly demonstrated the higher longevity of S-nZVI compared to nZVI upon exposure to anoxic waters, little has been done to assess the progressive structural changes of S-nZVI upon aging. As such we have limited insight into Fe^0 and/or FeS_m corrosion processes on S-nZVI surfaces nor do we know the parameters that accelerate or limit them. This understanding is critical to make accurate predictions about S-nZVI corrosion behavior and ultimately its long-term fate in groundwater settings.

To close this gap, we have performed high-resolution structural and compositional characterization of freshly synthesized S-nZVI and S-nZVI aged in anoxic artificial groundwater for up to 180 days using high resolution electron microscopy, high energy X-ray scattering and spectroscopic techniques. These observations were complemented with reactivity data, by determining TCE reduction rates for progressively aged S-nZVI. In addition, S-nZVI structural and reactivity changes were further assessed in TCE re-spiking experiments, to mimic S-nZVI fate in a contaminated subsurface. Finally, these data were used to build a conceptual model of S-nZVI redox sites and their stability and fate upon exposure to groundwaters, in order to predict S-nZVI performance in field scale applications.

2. Materials and methods

All syntheses, aging, and sample preparations for characterization were done inside an anoxic, vinyl-walled glove box (95% N_2 /5% H_2 ; Coy laboratories) using reagent grade chemicals (ESI,† Text S1) and deoxygenated, deionized water (MilliQ, resistivity > 18 Ω cm).

2.1 S-nZVI synthesis

Sulfidized nanoscale zerovalent iron (S-nZVI) synthesis was based on a modified procedure from Rajajayavel *et al.*⁴ in which nZVI was produced by reduction of FeCl_2 using sodium borohydride. The nZVI was reacted with a Na_2S solution in acetate-buffer (pH 6.0 ± 0.1) for 3 hours. The resulting S-nZVI particles were washed thrice with 96% ethanol, vacuum filtered, and then used for characterization, aging, and reactivity studies. Additional synthesis details are given in ESI,† Text S2.

2.2 S-nZVI aging experiments

The freshly synthesized S-nZVI particles were aged for up to 180 days (mass loading of 1 g L^{-1}) in 150 mL anoxic artificial groundwater (water composition given in ESI,† Table S1), prepared using a previously established procedure.¹⁰ The reactors were capped with Viton rubber stoppers and kept inside the anoxic glovebox without shaking throughout the aging process. Between 0 and 180 days, aliquots were removed to isolate the aged particles for structural and compositional characterization (ESI,† Text S3). To assess the reactivity of these progressively aged S-nZVI, identical S-nZVI groundwater aging reactors were set up as explained above. After specific aging times, a reactor was sacrificed and spiked with 110 μM TCE to initiate the reaction. Once the TCE was added, the decrease in TCE concentration was monitored over the following 50 hours using gas chromatography-mass spectroscopy (GC-MS) to derive reaction rates. Specific details are given in ESI,† Text S4, including set-up of controls and GC-MS measurement procedures.

In a separate reactor, freshly synthesized S-nZVI (mass loading of 1 g L^{-1} in 150 mL anoxic artificial groundwater) was exposed to 7 sequential 110 μM TCE amendments over a total of 11 days. Re-spiking of TCE occurred once the former injected TCE concentration was reduced to <5%. TCE removal was regularly monitored using GC-MS and rates for each re-spike were derived using identical protocols as explained for TCE reactivity experiments (ESI,† Text S4).

2.3 S-nZVI characterization

The bulk structure of S-nZVI was determined with synchrotron-based X-ray diffraction (XRD) and pair distribution function (PDF) analyses at beamline 11-ID-B (58 keV, $\lambda = 0.2114 \text{ \AA}$) at the Advanced Photon Source, Argonne National Laboratory (USA).^{8,11} The S-nZVI surface composition was determined with X-ray photoelectron spectroscopy (XPS) using a Kratos Axis Ultra^{DLD} with a monochromated Al $K\alpha$ X-ray source ($h\nu = 1486.6 \text{ eV}$, power = 150 W), pass energy of 20 eV and analysis spot size of about $700 \mu\text{m} \times 300 \mu\text{m}$. The size, morphology, and spatial chemical composition of S-nZVI were characterized by transmission electron microscopy (TEM) and scanning electron microscopy (SEM). The TEM images, selected area diffraction patterns (SAED), as well as electron dispersive X-ray (EDX) spectra and elemental maps were acquired using

an FEI Tecnai G20 F20 X-Twin FEG S/TEM operated at 200 kV and equipped with a Gatan imaging filter (GIF) Tridiem™, a Fischione high angle annular dark field (HAADF) detector and an EDAX X-ray analyzer. SEM images were acquired using FEI Quanta 3D FEG SEM at 7 kV and 8.7 pA using a secondary electron detector. Full details of sample handling, data measurement and analyses are given in ESI,† Text S3.

3. Results and discussions

3.1 Structure of initial S-nZVI

In synchrotron XRD patterns ($I(Q)$), unaged S-nZVI exhibits broad peaks at 3.09 \AA^{-1} (2.03 \AA) and 5.35 \AA^{-1} (1.17 \AA), which correspond to the (110) and (211) planes of nanocrystalline α -Fe (*i.e.*, Fe^0 core, Fig. 1a).¹² An additional smaller peak exists at $\sim 1.19 \text{ \AA}^{-1}$ (5.28 \AA), matching the (001) reflection of mackinawite (FeS_m) but with a $\sim 5\%$ expanded basal plane spacing, relative to a nanocrystalline mackinawite (Fig. 1a),^{13,14} as previously observed for these materials using XRD.² The PDFs were extracted from the $I(Q)$ to determine the interatomic distances (Fig. 1b). Overall, the PDF of S-nZVI resembles the pattern for the non-sulfidized ZVI, where the peaks for the first ($r = 2.48 \text{ \AA}$) and second ($r = 2.56 \text{ \AA}$) shell Fe^0 - Fe^0 are broadened and cannot be readily distinguished,⁸ indicative of local disorder in the structure of the Fe^0 core. Oscillations decay quickly with increasing r -value, showing that long range order was limited. To isolate the PDF of the shell, a differential PDF (d-PDF) was extracted by subtracting the PDF of nZVI from that of S-nZVI (Fig. 1c).^{8,15,16} The d-PDF exhibits peaks at positions matching a synthetic mackinawite (Fig. 1c).^{17–19} This implies that while its interlayer was expanded slightly (*i.e.*, $\sim 5\%$ increased basal spacing), its local atomic configuration within the layers maintained the mackinawite-like structure.^{20,21}

TEM images of freshly prepared S-nZVI show spherical particles of high contrast about 50–150 nm in size (Fig. 2a). The majority of the particles were coated by a shell of less electron dense material about $\sim 5 \text{ nm}$ thick (Fig. 2b). EDX

maps reveal that the shell material contained both Fe and S (Fig. 2c) and selected area electron diffraction (SAED) only shows reflections for Fe^0 and FeS_m (ESI,† Fig. S2). At high resolution, parts of the shell show lattice fringes with d -spacings of $5.4 \pm 0.2 \text{ \AA}$ (Fig. 2d), similar to the expanded (001) FeS_m reflection in $I(Q)$ (Fig. 1a).²² Moreover, the FeS_m crystals were often curving around the Fe^0 core, and oriented to expose its (001) surface to the bulk solution (ESI,† Fig. S3). Other parts of the shell exhibit FeS_m layers with no apparent structural coherence (ESI,† Fig. S3), an indication of defects in the shell. In addition, the shell in places showed a sheet-like morphology and different crystal orientations (Fig. 2e), with a d -spacing value of $3.1 \pm 0.1 \text{ \AA}$ appearing in 2D fast Fourier transforms (Fig. 2e, inset). This distance is consistent with FeS_m (011) plane,²³ which may indicate that the observed sheet-like morphology are oriented perpendicular to the electron beam. This variability in crystal orientation along with the observed lattice mismatches implied a degree of heterogeneity in the FeS_m shell architecture.

In summary, our characterization reveals that the shell of freshly synthesized S-nZVI was composed of a $\sim 5 \text{ nm}$ thick FeS_m layer with expanded interlayers surrounding the Fe^0 core. While the FeS_m shell surface dominantly exposes its (001) surface, parts of the FeS_m shell exhibit structural discontinuities, caused by defects and variability in crystal orientations. This shell architecture is distinct from that of sulfidized ZVI particles produced *via* the one-pot dithionite synthesis, which was observed to be substantially thicker, more flakey and dominated by amorphous ferrous hydroxide (white rust) with some amorphous FeS close to the Fe^0 core interface.^{3,8,24}

3.2 S-nZVI aged in anoxic artificial groundwater

The continued exposure of S-nZVI to anoxic artificial groundwater led to progressive structural and compositional changes as shown by XRD, PDF and XPS (Fig. 3a–d). In XRD patterns, peaks from the Fe^0 core decrease in intensity with

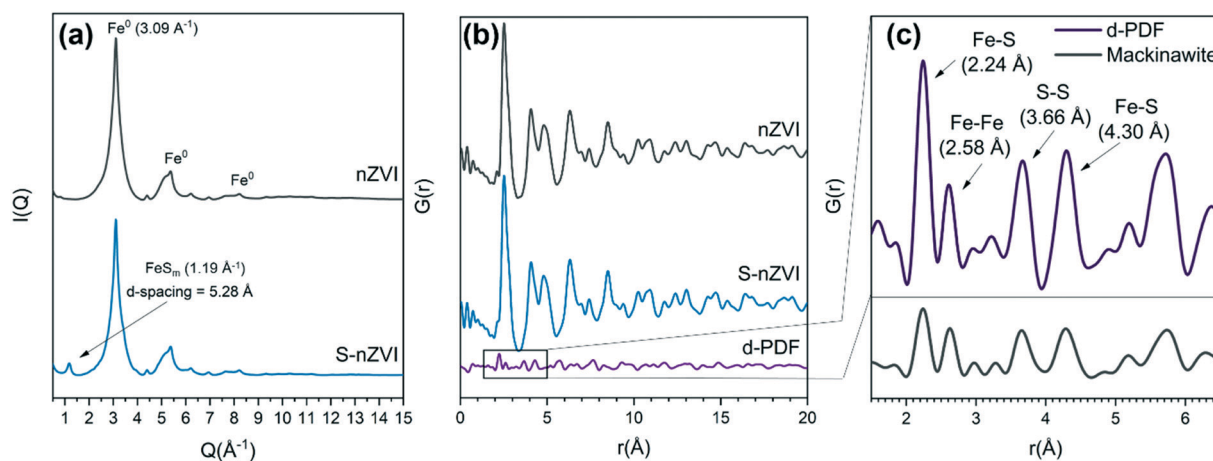


Fig. 1 (a) $I(Q)$ and (b) PDFs of sulfidized and non-sulfidized zerovalent iron (S-nZVI and nZVI). (c) d-PDF (= $\text{PDF}_{\text{S-nZVI}} - \text{PDF}_{\text{nZVI}}$) showing pair correlations that match a mackinawite-like phase. The PDF of synthetic pure mackinawite is given as reference.

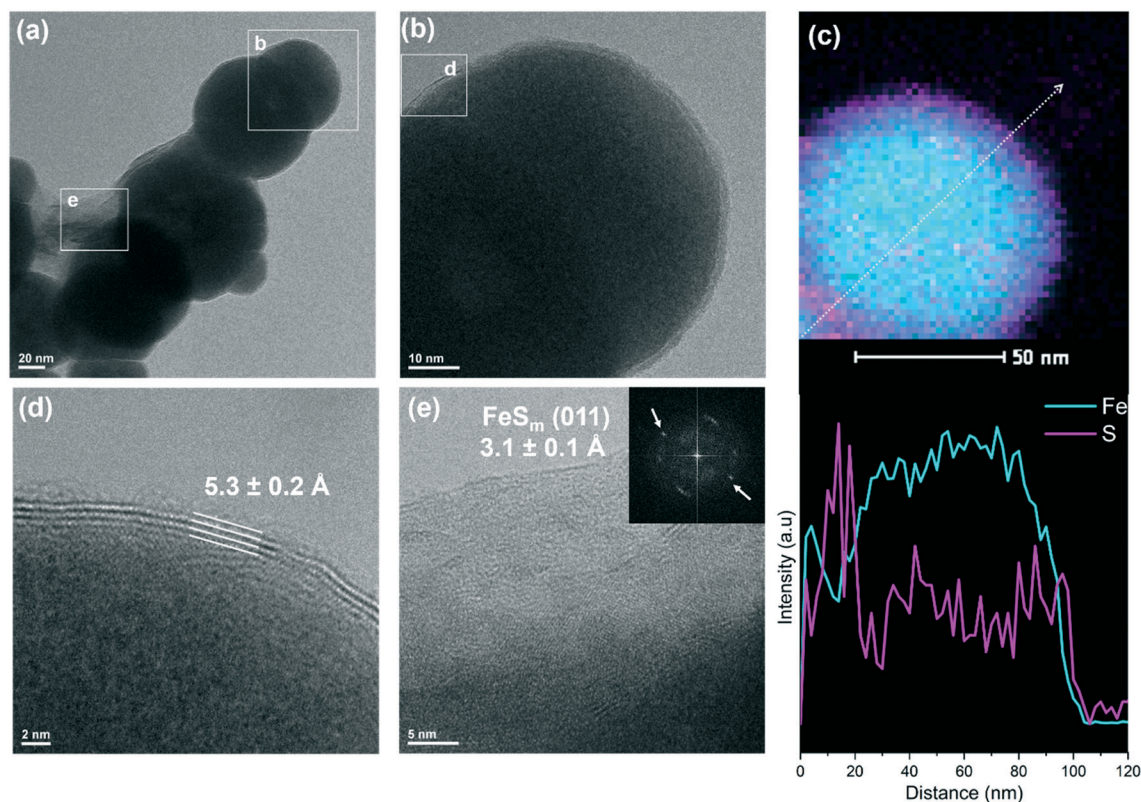


Fig. 2 TEM and EDX analyses of freshly synthesized S-nZVI. (a) S-nZVI aggregate showing particle size distribution and areas where high-resolution analyses were performed. (b) S-nZVI particle showing electron dense core surrounded by ~ 5 nm thick, less electron dense shells. (c) EDX map (top) and line intensity profile (bottom) normalized to unity of an isolated particle confirm the Fe-rich core, surrounded by a shell enriched in both sulfur and iron.^{7,24} (d) Lattice fringes in the shells have d -spacings consistent with the $I(Q)$ peak for FeS (001).²² (e) Isolated area showing FeS_m crystal orientation leading to lattice fringes with d -spacing consistent with (011).

material age while peaks associated with carbonate green rust (GR_{CO₃}) and white rust (WR) increase (Fig. 3a). Consistent with XRD, PDFs show a progressive increase in Fe^{II/III}-O (~ 2.11 Å) and Fe^{II}-Fe^{II/III} (~ 3.19 Å) distances stemming from the formation of corrosion products (*i.e.*, GR_{CO₃}, WR, Fig. 3b), while the peak intensity for the Fe⁰-Fe⁰ distance decreases (*e.g.*, 2.53 Å, Fig. 3b). Using these relative changes in PDF peak intensities, we have approximated the decrease in Fe⁰ core material with aging (details of results in ESI,† Table S3 and Fig. S4; methods in Text S3). Over the first 10 days of aging, no significant changes in Fe⁰-Fe⁰ PDF peak heights are observed, suggesting that Fe⁰ oxidation (*i.e.*, corrosion) was negligible. From day 10 to 60, the Fe⁰-Fe⁰ peak progressively decreased, indicating the decrease in molar fraction of Fe⁰ to about 50% of its initial amount due to corrosion from aging. From day 60 to 120, only slight additional corrosion occurred. In comparison, corrosion of nZVI started instantaneously and occurred substantially faster, with almost 80% of the Fe⁰ oxidized after 60 days (ESI,† Fig. S5 and S6).

These progressive structural changes are also evident in the observed surface compositional changes based on our XPS data. The Fe 2p_{3/2} spectra (Fig. 3c) show a progressive decrease in Fe²⁺-S/Fe⁰ species (peak at binding energy, BE = ~ 706 eV), while Fe²⁺-O species (broad peak at BE = ~ 710 eV)

increase with aging (ESI,† Table S4). Similarly, peaks for S²⁻ species (BE = ~ 161 eV) in the S 2p spectra gradually decrease (Fig. 3d), while the intensity for SO₄²⁻ species (BE = ~ 169 eV) progressively increases (ESI,† Table S5). Peak deconvolution of the S 2p spectra shows that the amount of transient sulfur species (*i.e.*, S_n²⁻, S(0), S₂²⁻) was fairly constant with aging time (*i.e.*, consistently below 12% of total surface sulfur, ESI,† Table S5). This could suggest that transient sulfur species did not evolve from S²⁻ oxidation by aging. These species may have likely formed from oxidation due to quick exposure (<1 minute) of the samples to ambient atmosphere during transfer to the XPS sample entry chamber.²⁵ Given that no systematic changes in transient sulfur species were measured, the observed increase in SO₄²⁻ is most likely linked to SO₄²⁻ adsorption from bulk solution (0.25 mM SO₄²⁻ initially present) by the corrosion products that progressively formed upon aging (ESI,† Table S6).²⁶ Similarly, the observed progressive decrease in S²⁻ peak intensity is caused by the gradual increase in voluminous corrosion products, which systematically decreased the amount of S-nZVI that were detected within the area of analysis (*i.e.*, S species; Table S6†).

It is predicted that with continued S-nZVI aging, Fe⁰ corrosion processes would certainly proceed but at much lower rates seeing that little structural changes occurred between 60 and 120 days. To visualize the effects of continued

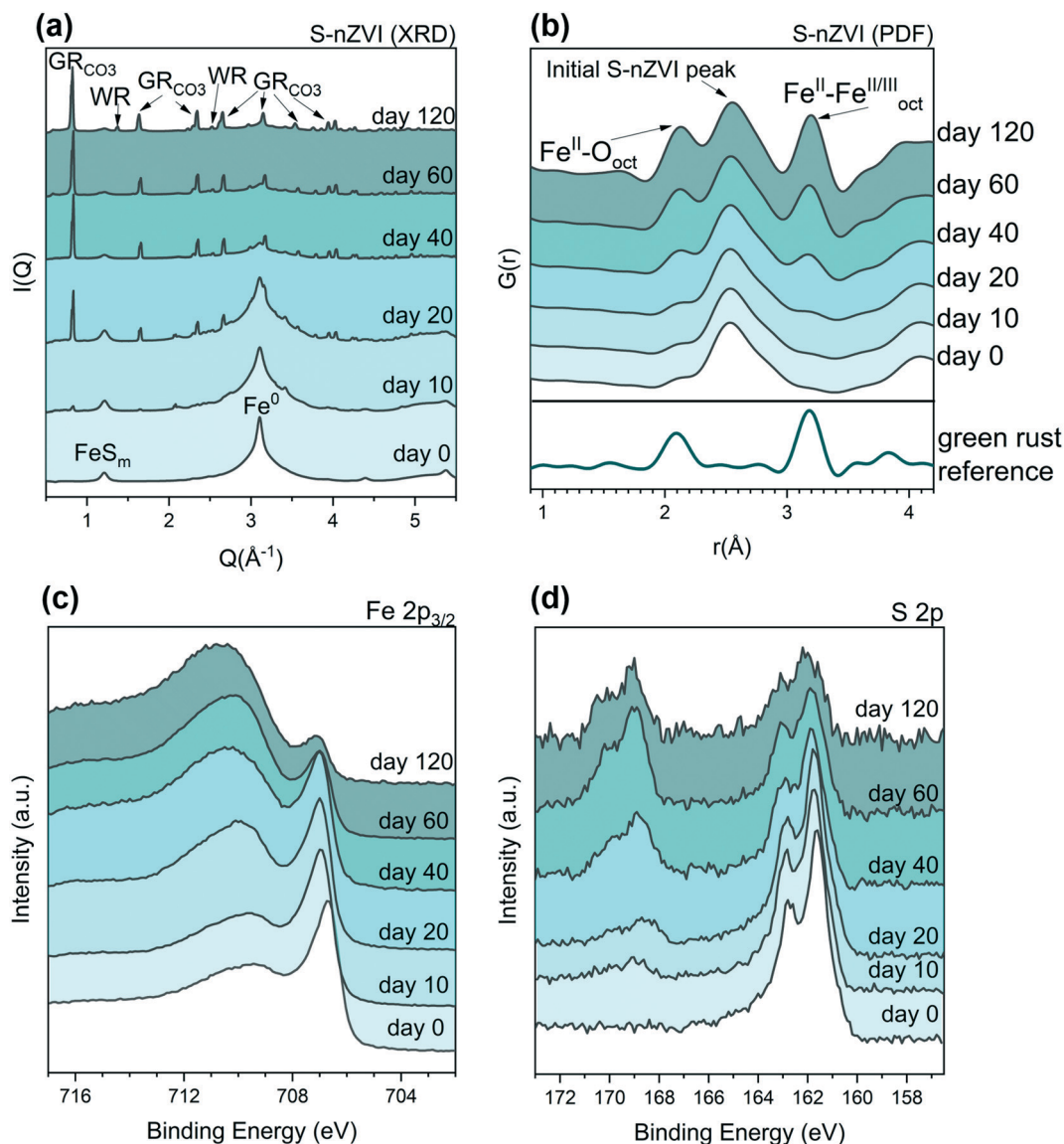


Fig. 3 (a) XRD patterns of S-nZVI aged in artificial groundwater showing the gradual formation of secondary carbonate green rust (GR_{CO_3}) and white rust (WR). (b) PDF patterns show changes in the local coordination of S-nZVI upon aging for 120 days. A PDF of green rust is also shown to ease identification of the developing $\text{Fe}^{\text{II/III}}\text{-O}$ and $\text{Fe}^{\text{II}}\text{-Fe}^{\text{II/III}}$ distances. XPS spectra of (c) Fe 2p_{3/2} and (d) S 2p, showing changes in surface Fe and S species as a function of aging time.

aging, TEM imaging and EDX elemental mapping were performed on S-nZVI particles after 180 days of aging (Fig. 4). Compared to the initial material (Fig. 2a), the aged particles show “hollow” cores, seemingly devoid of electron dense material (*i.e.*, little contrast remained), while the shell (*i.e.*, interface) appears intact with some parts having laminar or sheet-like structures (Fig. 4a and b). EDX mapping and normalized line intensity profiles of the “hollow” particles show low Fe signals for the core but high Fe and S signals for the shell (Fig. 4c). At higher resolution, particle cores exhibit variations in contrast (Fig. 4b and d), suggesting that material loss occurred heterogeneously within a single particle, and also differed among particles. Closer inspection of the shell show that the (001) mackinawite-like planes are still present, even after 180 days aging ($d = 5.2 \pm 0.2 \text{ \AA}$, Fig. 4e). Similarly,

the SAED pattern of the aged particles exhibit patterns that may be indexed to a mackinawite-like phase with extended d -spacings (ESI,† Fig. S7). In agreement with XRD, PDF and XPS, both SEM and TEM analyses suggest that GR_{CO_3} is the main corrosion product (Fig. 5). In addition, SEM and TEM images show that GR_{CO_3} formed micron-sized, hexagonal platelets that seem spatially separated from S-nZVI particles.

In terms of TCE reactivity, all aged S-nZVI fully reduced the initially added $110 \mu\text{M}$ TCE within 50 hours (ESI,† Fig. S8), but aging time affected the reduction rate. Within the first 10 days of aging, the rate constant (k_{obs}) minimally changed ($\sim 0.17 \text{ h}^{-1}$, ESI,† Table S7). It then decreased from 0.16 to 0.12 h^{-1} for S-nZVI aged from 20 to 60 days, before stabilizing around a value of 0.10 h^{-1} after 120 days of aging. Despite this decline in S-nZVI reduction rate over 4 months,

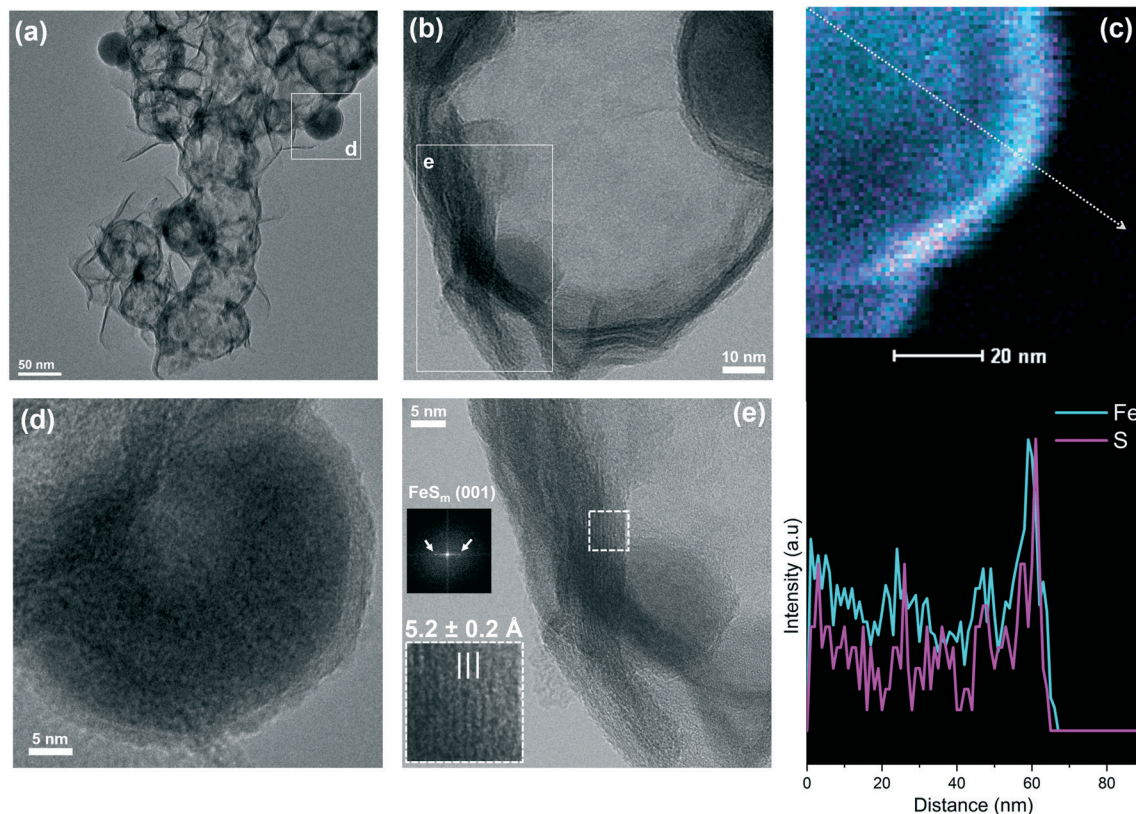


Fig. 4 TEM and EDX analyses of S-nZVI particles that were aged for 180 days in anoxic artificial groundwater. (a) An aggregate of aged S-nZVI particles. (b) A particle showing a “hollow” core surrounded by an intact mackinawite-like shell. (c) EDX map (top) and the line intensity profiles of Fe and S normalized to unity (bottom). (d) High resolution TEM image of a particle with substantial core material and a ~ 5 nm shell with fringes. (e) High resolution TEM image of an isolated shell structure showing lattice fringes ($d = 5.2 \pm 0.2$ Å, inset) that match the basal-spacing of the (001) FeS_m features observed for unaged S-nZVI (Fig. 2d). This is further confirmed by the FFT of the same image.

the material is still highly reactive; particularly when comparing to nZVI aging results in our previous study, where TCE reduction became negligible after 7 days aging of nZVI under identical conditions.⁸

3.3 S-nZVI aged by re-spiking with TCE

Over 11 days, 1 g L^{-1} S-nZVI suspended in the groundwater matrix was exposed to 7 TCE re-spikes (each $110 \mu\text{M}$). The TCE was continuously and rapidly degraded by S-nZVI, with rates progressively decreasing with each re-spike (ESI[†] Fig. S9 and Table S8). XRD and PDF characterization of the solids at the end of the 7th TCE re-spike showed the presence of GR_{CO_3} and magnetite (M) as corrosion products (ESI[†] Fig. S10 and S12), and a clear depletion in Fe core material by $\sim 21\%$ (based on PDF peak analyses), which matched well with the theoretical electron consumption of $\sim 25\%$ (based on added S-nZVI and TCE and assuming an average consumption of 6 electrons to fully reduce one TCE molecule).²⁸ These data further show that the FeS_m shell was still apparent (*i.e.*, peak at 1.19 \AA^{-1} , ESI[†] Fig. S10) and that no other iron sulfide phases could be detected. Overall, the observed changes in structure and reactivity upon TCE re-spiking are very similar to aging in anoxic groundwater alone (section 3.2). However,

these changes occurred at different rates. For the groundwater aging experiments, little if any structural changes were observed over the first 10 days; whereas in a similar time span, changes were observed in the re-spiking experiments, indicating that TCE was the main oxidant and responsible for Fe^0 oxidation in the re-spiking experiment (Fig. S11[†]). Lastly, despite the presence of a stronger oxidant in these experiments (*i.e.*, TCE), synchrotron-based XRD indicates that the shell structure was unaffected, with no signs of shell oxidation and/or re-crystallization.

3.4 Conceptual model of S-nZVI redox sites and their fate with aging

Overall, our experiments in simulated anoxic groundwater showed that:

i) Core corrosion of S-nZVI occurred slower in the absence of a strong oxidant (*e.g.*, TCE, Fig. 3b and S4[†]) in comparison to reactions where TCE is continuously present (Fig. S11[†]), allowing it to conserve its electron pool (*i.e.*, reactivity) for prolonged periods. In comparison, nZVI exhibited rapid core corrosion by anoxic artificial groundwater (Fig. S6[†]), as well as almost complete reactivity loss after only 7 days, as shown in our previous study.⁸

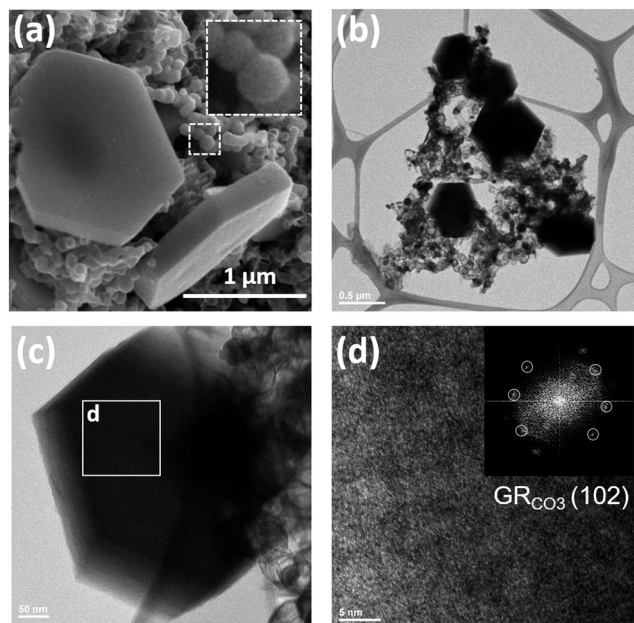


Fig. 5 SEM and TEM analyses of 180 days aged S-nZVI. (a) SEM image shows large, hexagonal crystal platelets characteristic of carbonate green rust (GR_{CO_3}) and spherical S-nZVI particles (inset). (b) Low resolution TEM image of GR_{CO_3} platelets surrounded by aged S-nZVI. (c) HR-TEM of GR_{CO_3} showing area where (d) FFT image was obtained. The FFT pattern matches (102) plane of GR_{CO_3} with d -spacing = 2.6 Å.²⁷

ii) There is no indication that the FeS_m shell underwent re-crystallization and/or oxidation, whether exposed to TCE or anoxic artificial groundwater. This is in contrast to previous S-nZVI aging studies, which argued that the instability of the shell controls reactivity loss.⁶ Our results, however, are more consistent with another study on pure mackinawite systems, where the authors demonstrated the stability of the mackinawite structure even after 106 days of aging in a highly reducing and alkaline aqueous environment.²⁹

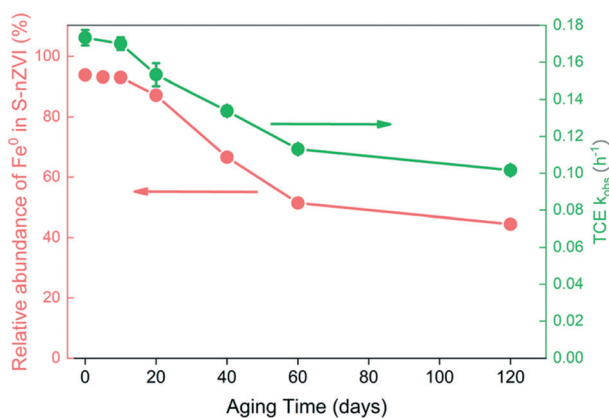
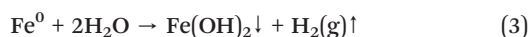
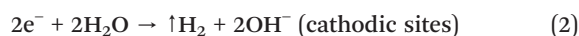


Fig. 6 The decrease in S-nZVI Fe^0 content (in red) and TCE reduction rate constant, k_{obs} , (in green) as a function of aging time. The error bars represent the standard error of the fitted k_{obs} from linear regression calculations (Fig. S8†).

iii) The observed decrease in TCE k_{obs} with aging time seemed to follow the depletion in the Fe^0 core volume (Fig. 6), suggesting that the cause of the decrease in TCE reactivity likely stems from the loss in Fe^0 . Previous studies have proposed that shell re-crystallization and precipitation of corrosion products on the surface cause the decrease in k_{obs} .^{6,30,31} Our characterization showed that the corrosion products formed external to S-nZVI particles aged in anoxic artificial groundwater (Fig. 5). These observations may indicate that k_{obs} values are likely also influenced by the Fe^0 core content and the specific corrosion pathways, which in turn control type and location of secondary mineral formation.

To create a conceptual model of the active redox sites on S-nZVI surfaces that is consistent with our observations, let us first consider the case of aging in groundwater (without TCE present). The formation of hollow S-nZVI particles, with depleted Fe^0 cores and intact shell structures, has been observed once before for S-nZVI (two-step synthesis, Na_2S precursor) when it was reacted with pertechnetate (TcO_4^-) for 2 months.² The authors linked this transformation to nanoscale Kirkendall effect based on similarities to structures observed for Cu^0 nanoparticles transformed under sulfate reducing conditions.^{2,32} However, such a process seems unlikely in our aging experiments because solid state diffusion *via* Kirkendall effect typically requires elevated temperatures since the reaction is kinetically limited at ambient temperatures.³³ If not by solid state diffusion, the generated Fe^{2+} must have been able to transfer into bulk solution by some other mechanisms. This is because we do not see any clear evidence for localized corrosion product formation inside these aged “hollow” S-nZVI particles. Close examination of the FeS_m shell showed numerous shell defects and plane boundaries, which indicate that the shell exhibits “weak” points, where diffusion processes could occur more easily, *i.e.*, allowing for water and ions to access the Fe^0 core. Indeed, such a scenario is supported by our groundwater aging results, where little corrosion occurred in the first 10 days. However, after prolonged incubation (~10–20 days), which gave time for local dissolution and/or diffusion processes at these weak points, water started to interact with Fe^0 sites, leading to continued Fe^0 oxidation (*i.e.*, core depletion) from then onwards. In such a scenario, it is expected however, that these weak points should be quickly passivated by surface precipitates due to the concomitant occurrence of anodic (eqn (1)) and cathodic reactions (eqn (2)) that favors $\text{Fe}(\text{OH})_2$ (white rust) formation (eqn (3)):



There is no clear indication of surface passivation in SEM and TEM images and we see continued high TCE reactivity

by the aged S-nZVI. Thus, for continued Fe^0 core depletion without substantial internal mineral formation, we propose that the anodic and cathodic sites must have been locally separated on the S-nZVI surface. The separation allows for localized acidification and dissolution at anodic sites; and localized basic conditions and H_2 evolution at the cathodic sites. At the anodic sites, the acidification caused the eventual opening of the shell weak points, which led to more favorable Fe^{2+} diffusion conditions towards the bulk solution. We presume that the Fe^{2+} diffusion during aging is possible because of the high Fe^{2+} concentration gradient between the area of local anodic sites and the bulk solution. To sum up, in the absence of a strong oxidant (*i.e.*, contaminant), water can eventually penetrate weak points in the FeS_m shell (*i.e.*, access Fe^0 sites) to form anodic and cathodic sites. However, for gradual Fe^0 core depletion to occur as observed here, and without clear indications for corrosion products inhibiting the process, these reactions (eqn (1) and (2)) must occur at different weak sites, mimicking a galvanic-like corrosion condition. Noteworthy, this mechanism holds true if the rate of water reduction at FeS_m sites is low. We believe this is true because numerous studies have shown that the presence of FeS_m sites suppressed H_2 formation in comparison to non-sulfidized ZVI.^{4,6,34,35} This is further corroborated by our own results where we see little if any corrosion within the first 10 days of aging in anoxic artificial groundwater.

A last point to discuss in relation to corrosion mechanism is the observed heterogeneity in Fe^0 core content after 180 days of aging. Seeing almost completely “hollow” particles (Fig. 4b), along with particles that retained parts or most of their initial Fe^0 core (Fig. 4d), suggest that the FeS_m shell “weak” points (*i.e.*, the number of shell structural discontinuities) varies amongst particles. As such, S-nZVI that exhibit shells with a high number of “weak” points likely corrode first and faster, while S-nZVI with lower shell heterogeneities are able to preserve their Fe^0 core thereby sustaining their reactivity with TCE for prolonged periods. Presumably, this could explain why Fe^0 corrosion and k_{obs} stabilized at the latter stage in groundwater aging experiments (*i.e.*, 60–120 days, Fig. 6) and why k_{obs} almost plateaued following the 4th TCE amendment in the re-spiking experiment (Fig. S9†).

In the case when TCE is consistently present, analogous to our re-spiking experiments, the general assumption is that the cathodic reaction (*i.e.*, TCE reduction) occurs at FeS_m sites while Fe^0 sites become oxidized. This is heavily supported by reactivity studies that show enhanced TCE degradation in the presence of an FeS_m shell.^{4,6} Moreover, it is argued that the FeS_m shell facilitates TCE sorption and reduction due to its enhanced hydrophobic and electron conductive properties.^{6,24,30,35} Our data support these assumptions. We reveal that the particle surface is often dominated by (001) FeS_m plane features, which are considered to be the most hydrophobic and conductive in comparison to other FeS_m planes.^{18,19,36–38} The reason for such conductivity stems from the similarity in Fe–Fe interatomic distance between FeS_m and

Fe^0 (body centered cubic),^{18,39,40} which is also evident in our d-PDF data (Fig. 1c). Moreover, our re-spiking experiments clearly showed that it is the Fe^0 core that gets oxidized, while the shell structure seems to remain intact, with no other FeS phases detected. This suggests that the core–shell architecture is robust and that in the presence of continued exposure to target contaminants, electron efficiency is achieved.²⁸

4. Environmental implications

Our data clearly showed that the longevity of S-nZVI is heavily dependent on the architecture and homogeneity of the FeS_m shell structure. Overall, prolonged and sustained S-nZVI reactivity is enabled by the persistent FeS_m shell providing hydrophobic and electron conductive sites for TCE reduction (cathodic reaction), while exhibiting a number of defect sites that facilitate the continuous but controlled Fe^0 core oxidation (anodic reaction). The spatial separation of anodic and cathodic sites in both reactivity scenarios (*i.e.*, after aging with and without TCE) is argued to be key to maintain S-nZVI reactivity as it allows for corrosion products (*i.e.* GRCO_3 , WR) to form external to S-nZVI surfaces, thereby limiting surface passivation. A point to consider, however, while a perfectly homogeneous FeS_m shell with minimal defects would seem to enable high S-nZVI longevity in groundwater settings (*i.e.*, limited corrosion by water), it may also decrease the sufficient “accessible” anodic sites (*i.e.*, Fe^0 oxidation sites), which ultimately increase the risk of surface passivation. Furthermore, while TCE can be quickly reduced at FeS_m sites, other chlorinated ethenes such as *cis*-DCE, which often co-exist with TCE in contaminant plumes, require Fe^0 sites for reduction.⁸ Thus, a balance between FeS_m shell features and target contaminant should also be assessed to realize an optimal *in situ* remediation.

The results shown here are a product of idealized and simplified scenarios. Therefore, other factors should also be considered such as specific groundwater chemistries (*i.e.*, specific ion effects, ion concentrations, pH conditions) and the presence of microbiomes that participate in sulfur and iron cycling;^{41,42} all of which may impact the stability of FeS_m or influence the corrosion rate of Fe^0 in S-nZVI. Additionally, consideration should also be given to understanding the synthesis controls of S-nZVI nanostructure during synthesis to further tailor its application to specific groundwater contaminants and in various types of subsurface environments.

Conflicts of interest

There are no conflicts to declare.

Acknowledgements

The authors thanks Olaf Borkiewicz and Kevin A. Beyer for support with X-ray total scattering measurements at APS beamline 11 ID-B, Argonne, USA. We also thank Richard Wirth for the assistance in TEM experimental set-up. This research was funded by Metal-Aid Innovative Training

Network (ITN), supported by a grant from the European Commission's Marie Skłodowska Curie Actions program under project number 675219. LGB and HMF also acknowledge financial support by the Helmholtz Recruiting Initiative (Award No. I-044-16-01). Part of the data was acquired at Advanced Photon Source, a U.S. Department of Energy (DOE) Office of Science User Facility operated for the DOE Office of Science by Argonne National Laboratory under contract no. DE-AC02-06CH11357. Support for travel to the synchrotron facility came from the Danish Council for Independent Research (via DANSCATT).

References

- 1 E. C. Butler and K. F. Hayes, *Environ. Sci. Technol.*, 2001, **35**, 3884–3891.
- 2 D. Fan, R. P. Anitori, B. M. Tebo, P. G. Tratnyek, J. S. L. Pacheco, R. K. Kukkadapu, M. H. Engelhard, M. E. Bowden, L. Kovarik and B. W. Arey, *Environ. Sci. Technol.*, 2013, **47**, 5302–5310.
- 3 E. J. Kim, J. H. Kim, A. M. Azad and Y. S. Chang, *ACS Appl. Mater. Interfaces*, 2011, **3**, 1457–1462.
- 4 S. R. C. Rajajayavel and S. Ghoshal, *Water Res.*, 2015, **78**, 144–153.
- 5 J. Xu, Y. Wang, C. Weng, W. Bai, Y. Jiao, R. Kaegi and G. V. Lowry, *Environ. Sci. Technol.*, 2019, **53**, 5936–5945.
- 6 D. Fan, G. O'Brien Johnson, P. G. Tratnyek and R. L. Johnson, *Environ. Sci. Technol.*, 2016, **50**, 9558–9565.
- 7 D. Fan, Y. Lan, P. G. Tratnyek, R. L. Johnson, J. Filip, D. M. O'Carroll, A. Nunez Garcia and A. Agrawal, *Environ. Sci. Technol.*, 2017, **51**, 13070–13085.
- 8 M. Mangayayam, K. Dideriksen, M. Ceccato and D. J. Tobler, *Environ. Sci. Technol.*, 2019, **53**, 4389–4396.
- 9 A. Liu, J. Liu, J. Han and W. X. Zhang, *J. Hazard. Mater.*, 2017, **322**, 129–135.
- 10 E. J. Smith, W. Davison and J. Hamilton-Taylor, *Water Res.*, 2002, **36**, 1286–1296.
- 11 D. J. Tobler, J. D. Rodriguez-Blanco, K. Dideriksen, N. Bovet, K. K. Sand and S. L. S. Stipp, *Adv. Funct. Mater.*, 2015, **25**, 3081–3090.
- 12 R. W. Wyckoff, *Crystal Structures*, Interscience Publishers, New York, 1948, vol. 1.
- 13 D. Csákerényi-malasics, J. D. Rodriguez-blanco, V. Kovács, A. Re, L. G. Benning and M. Pósfai, *Chem. Geol.*, 2012, **294–295**, 249–258.
- 14 M. Wolthers, S. Van der Gaast and D. Rickard, *Am. Mineral.*, 2003, **88**, 2007–2015.
- 15 W. Li, R. Harrington, Y. Tang, J. D. Kubicki, M. Aryanpour, R. J. Reeder, J. B. Parise and B. L. Phillips, *Environ. Sci. Technol.*, 2011, **45**, 9687–9692.
- 16 R. Harrington, D. B. Hausner, N. Bhandari, D. R. Strongin, K. W. Chapman, P. J. Chupas, D. S. Middlemiss, C. P. Grey and J. B. Parise, *Inorg. Chem.*, 2010, **49**, 325–330.
- 17 D. J. Vaughan and M. S. Ridout, *J. Inorg. Nucl. Chem.*, 1971, **33**, 741–746.
- 18 D. Rickard and G. W. Luther, *Chem. Rev.*, 2007, **107**, 514–562.
- 19 A. Devey, R. Grau-Crespo and N. De Leeuw, *J. Phys. Chem. B*, 2008, **112**, 10960–10967.
- 20 A. Lennie, S. Redfern, P. Schofield and D. Vaughan, *Mineral. Mag.*, 1995, **59**(397), 677–683.
- 21 F. M. Michel, S. M. Antao, P. J. Chupas, P. L. Lee, J. B. Parise and M. A. A. Schoonen, *Chem. Mater.*, 2005, **17**(25), 6246–6255.
- 22 A. Matamoros-Veloza, O. Cespedes, B. R. G. Johnson, T. M. Stawski, U. Terranova, N. H. de Leeuw and L. G. Benning, *Nat. Commun.*, 2018, **9**, 1–7.
- 23 A. Matamoros-Veloza, T. M. Stawski and L. G. Benning, *Cryst. Growth Des.*, 2018, **18**, 6757–6764.
- 24 S. Song, Y. Su, A. S. Adeleye, Y. Zhang and X. Zhou, *Appl. Catal., B*, 2017, **201**, 211–220.
- 25 S. Boursiquot, M. Mullet, M. Abdelmoula, J.-M. Génin and J.-J. Ehrhardt, *Phys. Chem. Miner.*, 2001, **28**, 600–611.
- 26 J. B. Harrison and V. E. Berkheiser, *Clays Clay Miner.*, 1982, **30**, 97–102.
- 27 H. Drissi, Ph. Refait and J.-M. R. Genin, *Hyperfine Interact.*, 1994, **90**, 395–400.
- 28 F. He, Z. Li, S. Shi, W. Xu, H. Sheng, Y. Gu, Y. Jiang and B. Xi, *Environ. Sci. Technol.*, 2018, **52**, 8627–8637.
- 29 L. G. Benning, R. T. Wilkin and H. L. Barnes, *Chem. Geol.*, 1999, **167**, 25–51.
- 30 D. Li, Z. Mao, Y. Zhong, W. Huang, Y. Wu and P. Peng, *Water Res.*, 2016, **103**, 1–9.
- 31 H. Dong, C. Zhang, J. Deng, Z. Jiang, L. Zhang, Y. Cheng, K. Hou, L. Tang and G. Zeng, *Water Res.*, 2018, **135**, 1–10.
- 32 F. A. Weber, A. Voegelin, R. Kaegi and R. Kretzschmar, *Nat. Geosci.*, 2009, **2**, 267–271.
- 33 A. Cabot, V. F. Puentes, E. Shevchenko, Y. Yin, L. Balcells, M. A. Marcus, S. M. Hughes and A. P. Alivisatos, *J. Am. Chem. Soc.*, 2007, **129**, 10358–10360.
- 34 J. Oudar, *Catal. Rev.: Sci. Eng.*, 1980, **22**, 171–195.
- 35 Y. Han and W. Yan, *Environ. Sci. Technol.*, 2016, **50**, 12992–13001.
- 36 N. Y. Dzade, A. Roldan and N. H. De Leeuw, *J. Phys. Chem. C*, 2016, **120**, 21441–21450.
- 37 N. Y. Dzade, A. Roldan and N. H. De Leeuw, *J. Chem. Phys.*, 2013, **139**, 124708.
- 38 N. Y. Dzade, A. Roldan and N. H. De Leeuw, *J. Chem. Phys.*, 2015, **143**, 094703.
- 39 M. Wolthers, L. Charlet, P. van Der Linde, D. Rickard and C. van Der Weijden, *Geochim. Cosmochim. Acta*, 2005, **69**, 3469–3481.
- 40 W. M. Skinner, H. W. Nesbitt and A. R. Pratt, *Geochim. Cosmochim. Acta*, 2004, **68**, 2259–2263.
- 41 T. M. Flynn, E. J. O. Loughlin, B. Mishra, T. J. Dichristina and K. M. Kemner, *Science*, 2014, **344**, 1039–1043.
- 42 K. P. Nevin and D. R. Lovley, *Environ. Sci. Technol.*, 2000, **34**, 2472–2478.